RSC Advances

ROYAL SOCIETY OF CHEMISTRY

www.rsc.org/advances

One-step synthesis of ordered mesoporous $CoAl_2O_4$ spinel based metal oxides for CO_2 reforming of CH_4

Leilei Xu [a, b], Jian Zhang [a], Fagen Wang [a, d], Kaidi Yuan [c], Liangjun Wang [c], Kai Wu [b, e], Guoqin Xu [a, b, d], Wei Chen [a, b, c, d]*

[a] Department of Chemistry, National University of Singapore, 3 Science Drive 3, 117543, Singapore

[b] Singapore-Peking University Research Center for a Sustainable Low-Carbon Future, 1 CREATE Way, #15-01, CREATE Tower, Singapore 138602, Singapore

[c] Department of Physics, National University of Singapore, 2 Science Drive 3, 117551, Singapore

[d] National University of Singapore (Suzhou) Research Institute, Suzhou, China

[e] College of Chemistry and Molecular Engineering, Peking University, Beijing 100871, China

*Corresponding author: Tel: 65-6516 2921; Fax: 65-6777 6126.

E-mail: phycw@nus.edu.sg

Abstract

A series of ordered mesoporous $CoAl_2O_4$ spinel based metal oxides with different Co content facilely synthesized via one-step evaporation induced self-assembly method were utilized as the catalysts for CO_2 reforming of CH_4 reaction. These mesoporous catalysts with unique textural property and outstanding thermal stability possessed excellent catalytic performances under various reaction conditions. The present catalysts with ordered mesostructure could provide sufficient accessible Co active sites for gaseous reactants and stabilize the Co metallic nanoparticles via the confinement effect of the mesoporous frameworks. These mesoporous catalysts performed better anti-coke ability than the non-mesoporous catalysts as well as traditional supported catalysts, promising a series of potential catalyst candidates for CO_2 reforming of CH_4 reaction.

Keywords: ordered mesoporous; $CoAl_2O_4$ spinel; metal oxide; carbon dioxide reforming; methane

1. Introduction

In the past decades, the excessive use of fossil fuels has caused severe environmental problems such as the rising concentration of greenhouse gases (mainly CO_2) in atmosphere [1, 2]. How to efficiently reduce CO_2 has attracted worldwide attention recently. Moreover, CO_2 can be considered as a valuable and sustainable carbon source for the synthesis of value-added chemical fuels. Intensive research efforts have been devoted to the development of efficient CO_2 reduction and conversion technologies [3, 4]. Among the strategies proposed for converting CO_2 into higher energy intermediates, the heterogeneous catalysis based processes are of great interest for the ease of process scalability [5, 6]. Among them, the catalytic carbon dioxide reforming of methane (CRM, $CH_4(g) + CO_2(g) = 2CO(g) + 2H_2(g)$, $\triangle H_{298} = +247$ kJ/mol) has been considered as one of the most promising technologies for the large scale CO_2 reduction and utilization. Moreover, under this process, two greenhouse gases (CO_2 and CH_4) can be simultaneously transformed into value-added synthesis gas resource ($H_2 + CO$) [7-14].

In comparison with other synthesis gas production processes, such as steam reforming of methane (SRM, $CH_4 + H_2O = CO + 3H_2$, $\triangle H = +206$ kJ/mol) and partial oxidation of methane (POM, $2CH_4 + O_2 = 2CO + 4H_2$, $\triangle H = -44$ kJ/mol), the present CRM process can generate syngas with lower H_2/CO ratio close to unity (1/1), which is highly desirable for downstream chemical processes, such as hydroformylation, oxo synthesis, and so on [12, 15-17]. However, the highly endothermic nature of this CRM process requires the reaction to be carried out at high temperatures (> 600 ^oC) to achieve acceptable conversion rates. Under such high temperature, it can result in severe thermal sintering of the metallic active sites [11, 18]. The CRM process is often accompanied by some undesirable side reactions, such as methane decomposition reaction ($CH_4(g) = C(s) + 2H_2(g)$, $\triangle H_{298} = +75$ kJ/mol), Boudouard reaction ($2CO(g) = C(s) + CO_2(g)$, $\triangle H_{298} = -172$ kJ/mol), etc. Coke can be formed in these side reactions to passivate the active centers [9, 12, 17, 19]. Both factors can cause the rapid deactivation of the catalyst, limiting the CRM process for large-scale industry applications. Therefore, it is highly desirable to rationally design efficient catalyst with high resistance to thermal sintering and carbon deposition.

It has been widely reported that most of the group VIII transition metals are active towards the CRM reaction [12, 20-22]. Among these metals, noble metals (Pt, Rh, Pd, Ir, etc.) usually perform higher catalytic activity and anti-coke capacity than non-precious metals (such as Ni and Co). However, it is more practical to develop Ni and Co based catalysts for scalable commercial applications due to their lower cost and inherent availability [23-25]. Supported Ni catalysts have been widely investigated because of their high initial activity comparable with noble catalysts. However, Ni based catalysts are prone to carbon deposition over the catalyst surface due to its strong C-H bond cleavage ability, leading to the rapid catalyst deactivation and the blockage of the fixed bed reactor [7, 14, 23]. It was found that the introduction of Co into Ni based catalyst could significantly suppress the carbon deposition during CRM reaction [7, 19, 26-28]. Recently, it has been revealed that Co showed considerably interesting catalytic performance for the CRM reaction [11, 21, 29-31].

For Co based catalysts, it is also very challenging to prevent the catalyst deactivation derived from thermal sintering of the metallic active sites and carbon deposition [23]. Based on the thermodynamic calculation, the methane decomposition reaction could only be initiated at temperature above 553 ^{o}C and the Boudouard reaction could take place at temperature below 700 ^{o}C. Therefore, it is impossible to simultaneously inhibit the occurrence of these two carbon deposition reactions under typical CRM reaction conditions [12, 32]. Moreover, the anti-coke performance of the catalyst is closely related to the size of the Co metallic active sites. Large Co metal ensembles easily stimulate carbon deposition, and therefore, the thermal sintering of the metallic active sites plays an important role in carbon deposition during the CRM process [33-36]. However, under the typical CRM reaction conditions, sintering of the Co particles can easily take place, making it as a big challenge to restrict Co metallic active centers within nanometer size.

Traditionally, small particles can be obtained by impregnation of a porous support with large surface area in a precursor-containing solution [37, 38]. However, it is difficult to control the metal dispersion because the metallic particles have strong tendency to aggregate at high temperature [18]. Intensive research efforts have been made to confine Co active sites in precursors with defined structures, such as spinel ($CoAl_2O_4$) and solid solution (Co-Mg-O) [34, 39, 40]. Because of the formation of a strong interaction between Co and the lattice structure, this can significantly improve the anti-sintering performance of the Co active centers. However, these materials usually could not provide enough accessible surface Co active sites since most of the active metal species are homogeneously dispersed in the bulk.

In order to address these challenges, a series of ordered mesoporous $CoAl_2O_4$ spinel based metal oxides with different Co content were firstly designed and facilely synthesized via one-step evaporation induced self-assembly method. These catalysts possess outstanding structural property and thermal stability. The Co species were homogeneously dispersed among the mesoporous matrix in the form of $CoAl_2O_4$ spinel, and thereby the Co nanoparticles could be effectively stabilized via its confinement effect. This can effectively suppress the severe sintering of Co nanoparticles under CRM conditions. Furthermore, these mesoporous catalysts with large surface areas, big pore volume, and uniform pore channels can ensure and provide sufficient Co active sites for the gaseous feedstock. These series materials promised ideal catalysts towards CRM reaction and even other catalytic reactions, such as CO_2 methantion.

2. Experimental

2.1. The synthesis of the ordered mesoporous $CoAl_2O_4$ spinel based metal oxide

Ordered mesoporous $CoAl_2O_4$ spinel based metal oxides with different Co containing were synthesized via one-step evaporation induced self-assemble (EISA) strategy [41, 42]. In a typical synthesis procedure, approximately 1.0 g $(EO)_{20}(PO)_{70}(EO)_{20}$ triblock copolymer (Pluronic P123, M_n = 5800, Sigma-Aldrich) was dissolved in 20.0 mL absolute ethanol with vigorous stirring. 1.6 mL of 67.0 wt% concentrated nitric acid, 10 mmol aluminum isopropoxide (98+%, Sigma-Aldrich), and quantitative $Co(NO_3)_2 \cdot 6H_2O$ (Sigma-Aldrich) were then sequentially added. The pink transparent homogeneous sol was transferred to a Perish dish after stirring for at least 5h at room temperature, and then put dish into a temperature and humidity controlled chamber at 60 °C with 50% relative humidity to undergo solvent evaporation for 48 h. A pink xerogel was obtained after EISA process. Calcination was carried out by slowly increasing temperature from room temperature to 700 °C with 1 °C/min ramping rate and maintaining at this temperature for 5 h in air. The final ordered mesoporous materials were labeled as OMA-*x*Co, where *x* referred to the molar percentage between Co and Al (x mol% = $n_{Co}/n_{Al} \times 100\%$, x = 3, 5, 7, 10, 15, n_{Al} = 10 mmol).

In order to investigate the role of ordered mesostructure in promoting catalytic property,

$CoAl_2O_4$ spinel based metal oxides without ordered mesostructure were also prepared. The obtained non-mesoporous materials were denoted as NPA-*x*Co, where the meaning of *x* was the same as that of OMA-*x*Co. The preparation method of NPA-*x*Co was similar to that of OMA-*x*Co, only without the addition of Pluronic P123 template.

To compare the catalytic properties of the present OMA-*x*Co catalysts with traditional supported catalyst, Co based catalyst supported on gamma-alumina (γ-Al_2O_3) was prepared via incipient wetness impregnation method using $Co(NO_3)_2 \cdot 6H_2O$ (Sigma-Aldrich) as the precursor of cobalt. After impregnation, the catalyst precursors were dried in a 60 °C oven for 24 h. Finally, the catalyst precursors were calcined at 700 °C for 5 h. The obtained catalysts were denoted as *x*%Co/Al_2O_3, where *x* also referred to the molar percentage between Co and Al.

2.2. Catalyst characterizations

X-ray diffraction (XRD) patterns were recorded on an X'pert Pro multipurpose diffractiometer (PANalytical, Inc., Netherlands) with Ni-filtered Cu Kα radiation (0.15046 nm). The N_2 adsorption and desorption analysis were measured using NOVA 2200e (Quantachrome, US) at -196 °C. Transmission electron microscopy (TEM) images, selected area electron diffraction (SAED), and energy-dispersed spectroscopy (EDS) measurements were performed on a JEOL 2010F microscope (Japan) under a working voltage of 200 KV. X-ray photoelectron spectroscopy (XPS) analyses of the catalysts were performed on a VG ESCALAB 210 (Thermo Scientific, US) spectrometer. The XPS data were referenced to the carbon species with C 1s at the binding energy of 284.8 eV. H_2 temperature programmed reduction (H_2-TPR) measurements for the as-prepared catalysts (100 mg) were performed on a ChemBET Pulsar TPR/TPD (Quantachrome, US) utilizing 5 mol% H_2/He steam (70 mL/min) as reducing agent and the hydrogen consumption was recorded using TCD detector. Temperature programmed hydrogenation (TPH) characterizations of the spent catalysts were carried out on the same apparatus as described for H_2-TPR. The long-term endurance-tested catalyst (30 mg) was submitted to a heat treatment (10 °C/min up to 900 °C) in a gas flow (60 mL/min) of the mixture 5 mol%H_2/He. Thermogravimetric (TG) analysis was performed by using TA instrument 2960 (Discovery, US) from room temperature to 900 °C with the heating rate of 10 °C/min under air stream.

2.3. Catalytic properties measurement

The reaction was performed in a vertical fixed bed quartz reactor at atmospheric pressure. The temperature of reaction bed was monitored by a coaxial thermocouple, which was protected by a small quartz thermocouple well. The flow rate of reactant gas was precisely regulated by mass flow controllers (Beijing Sevenstar Electronics Co.,Ltd., China). For each test, 100 mg catalyst was loaded on the quartz fixed–bed reactor. Prior to the reaction, the catalyst was pretreated by reducing in situ in a mixed flow of H_2 and N_2 (10/20 mL/min) with a heating rate of 1.5 ^{o}C/min rate to 800 ^{o}C, and maintained at 800 ^{o}C for 120 min. Before introducing in the reaction gases ($CH_4/CO_2 = 1$, without dilution), the catalyst bed was purged with N_2 for half an hour to remove the absorbed hydrogen. The reaction products were analyzed on line by the gas chromatograph (Agilent 7890B) equipped with automatic six-port valve and TCD detector. A TDX-01 packed column was used for the analysis of gaseous products. The conversions of the CO_2 and CH_4 were calculated based on the balance of carbon. Their formulas were listed as follows:

$$\mathrm{X}_{\mathrm{CH4}} = \frac{F_{in,CH4} - F_{out,CH4}}{F_{in,CH4}} \times 100\%$$

$$\mathrm{X}_{\mathrm{CO2}} = \frac{F_{in,CO2} - F_{out,CO2}}{F_{in,CO2}} \times 100\%$$

3. Results and discussion

3.1. Characterizations of the fresh catalysts

3.1.1. XRD analysis

Figure 1 (1) and (2) displayed the small-angle (0.5-5.0^{o}) and wide-angle (20-80^{o}) XRD patterns of the as-synthesized OMA-*x*Co catalysts calcined at 700 ^{o}C. As shown in the figure, each sample presented a strong diffraction peak around 0.8^{o} and another weak peak centered at around 1.4^{o}, respectively, implying the presence of *p6mm* hexagonal symmetry. Besides, most of samples possessed γ-Al_2O_3 (JCPDS Card No. 10–0425) and $CoAl_2O_4$ spinel (JCPDS Card No. 82–2252) diffraction peaks. It was worth noting that the intensity of the $CoAl_2O_4$ spinel diffraction peaks increased with the gradual increase of Co content from 3% to 15%. In contrast, the diffraction peaks for γ-Al_2O_3 became weaker until completely disappeared for OMA-15Co. It indicated that the incorporation of Co species into the framework is beneficial to the phase transformation toward $CoAl_2O_4$ by facilitating the following reaction: $CoO + Al_2O_3 = CoAl_2O_4$. However, it was very difficult to accurately calculate the crystallite size of $CoAl_2O_4$ spinel species by Scherrer formula due to the diffraction peak broadening, implying the high dispersion of Co species within the mesoporous skeleton.

The comparative studies for OMA-10Co, NPA-10Co, and 10%Co/Al_2O_3 catalysts prepared with different methods were also carried out and their XRD patterns were displayed in Figure 1 (3). The OMA-10Co synthesized with P123 template presented weak $CoAl_2O_4$ and γ-Al_2O_3 diffraction peaks; as a comparison, the NPA-10Co without template only displayed apparent $CoAl_2O_4$ diffraction peaks, which were much stronger than those of OMA-10Co in intensity. This suggested that the presence of P123 template was not favorable for the phase transformation toward $CoAl_2O_4$. For 10%Co/Al_2O_3 supported catalyst, it displayed characteristic diffraction peaks for Co_3O_4 (JCPDS Card No. 74–2120) species and γ-Al_2O_3 (JCPDS Card No. 10–0425), which could derive from the thermal decomposition of $Co(NO_3)_2\cdot 6H_2O$ precursor and γ-Al_2O_3 support, respectively. Moreover, the positions of the diffraction peaks of $CoAl_2O_4$ and Co_3O_4 crystalline phases almost overlapped, consistent with previous works [43-46]. $CoAl_2O_4$ and Co_3O_4 had the same spinel cubic (Fd3m) crystallographic structure only with slight difference in the lattice constant (a = 8.111 Å for $CoAl_2O_4$ and a = 8.0885 Å for Co_3O_4). Therefore, they displayed similar XRD peak patterns and the positions of the peak were nearly same. However, we expected that these catalysts would exhibit different Co2P XPS and H_2-TPR profiles due to the difference in their chemical coordination environments, which would be discussed later.

We also compared the XRD patterns of the as-reduced OMA-10Co, NPA-10Co, and 10%Co/Al_2O_3 catalysts at 800 °C for 2 h, as exhibited in Figure 1 (4). It could be observed that the intensities of metallic Co diffraction peaks (JCPDS Card No. 15–0806) for as-reduced OMA-10Co and NPA-10Co were weaker than those of 10%Co/Al_2O_3. For the as-reduced OMA-10Co, the diffraction peaks of $CoAl_2O_4$ disappeared; as a comparison, the intensities of γ-Al_2O_3 peaks became stronger after the reduction process. The process of $CoAl_2O_4$ reduction ($CoAl_2O_4 + H_2 = \gamma$-$Al_2O_3 + H_2O$) could account for it and the metallic Ni nanoparticles were highly dispersed within the mesoporous framework. However, for the as-reduced NPA-10Co, its main crystalline phase remained $CoAl_2O_4$ spinel and its diffraction peaks were much stronger than that of metallic Co. This suggests that the reduction of $CoAl_2O_4$ spinel species is more difficult.

The difference in reducibility between OMA-10Co and NPA-10Co could be attributed to their different structural properties. Compared with NPA-10Co, the OMA-10Co with larger surface area, bigger pore volume, and unblocked mesopore channel, made the reduction of $CoAl_2O_4$ spinel easier because the H_2 molecule is much easier to access surface species than the bulk material. The pattern of 10%Co/Al_2O_3 supported catalyst exhibited obvious metallic Co and γ-Al_2O_3 diffraction peaks, implying that most of Co_3O_4 species had been reduced.

3.1.2. Nitrogen adsorption-desorption analysis

The nitrogen adsorption-desorption isotherms and pore size distributions for the as-synthesized OMA-*x*Co with different Co molar fractions were displayed in Figure 2 (1) and (2), respectively. All the isotherms were attributable to the type IV with H1-shaped hysteresis loops, which were the typical characteristics for the presence of mesopores with cylindrical shape. For the adsorption isotherms with steep condensation steps, the corresponding pore size curves displayed very narrow steep condensation step, and the corresponding pore size distribution curves possessed narrow distribution around 10.0 nm.

In order to investigate the role of P123 template in constructing ordered mesoporous channels, the comparative analyses between OMA-10Co and NPA-10Co were carried out and the results were displayed in Figure 2 (3) and (4). Different with OMA-10Co with an IV H1-shaped hysteresis loop and a narrow pore size distribution, the NPA-10Co exhibited an IV H3-shaped hysteresis loop and a wide pore size distribution, suggesting the absence of uniform mesopores. This demonstrated that the P123 template played a crucial role in constructing ordered mesopores. Besides, the N_2 adsorption-desorption analysis result of 10%Co/Al_2O_3 supported catalysts were also depicted in Figure 2 (3) and (4), showing an IV H3-shaped hysteresis loop and a wide pore size distribution around 6.0 nm. It was proposed that the mesopores among 10%Co/Al_2O_3 might be stemmed from the disordered accumulation of γ-Al_2O_3 support particles. The values of specific surface areas, pore volumes, and average pore diameters of as-synthesized catalysts were summarized in Table 1. All the OMA-*x*Co samples calcined at 700 ^oC were provided with large BET surface areas up to 207.5 m^2/g, big pore volumes up to 0.31 cm^3/g, and average pore diameters in the range of 9.8-12.8 nm, which were much better than those of NPA-10Co and 10%Co/Al_2O_3.

In order to further verify the thermal stability of the ordered mesostructures of the OMA-*x*Co catalysts, the nitrogen adsorption-desorption analyses of the as-reduced OMA-*x*Co catalysts were also carefully carried out and their results were presented in Figure S1 (1) and (2) (Electronic Supplementary Information, ESI). Identical to their corresponding precursors, the as-reduced samples also fully displayed type IV isotherm with H1-shaped hysteresis loops and narrow pore size distributions around 10.0 nm, demonstrating excellent thermal stability. Besides, the isotherms and pore size distribution curves of the as-reduced NPA-10Co and 10%Co/Al_2O_3 were shown in Figure S1 (3) and (4) (ESI), respectively. Similar to the as-synthesized samples, they also possessed IV H3-shaped hysteresis loops and wide pore size distributions. These structural properties for the as-reduced catalysts were also summarized in Table 1. Compared with their corresponding precursors, the specific surface areas and pore volumes suffered some decline after the H_2 reduction treatment, which might be caused by the shrinkage of the skeleton and phase transformation at high temperature.

3.1.3. TEM analysis

In order to confirm the presence of the ordered mesoporous channels, TEM characterizations for OMA-*x*Co were carried out as displayed in Figure 3. For all the samples, the alignment of the cylindrical shaped pores along [1 1 0] direction were obviously observed. The SAED patterns of the ordered mesostructure domains were also provided as insets in Figure 3. Their diffraction rings were very fuzzy, indicating low crystallinity of the mesoporous walls. This was consistent with the previous XRD patterns that only exhibited weak diffraction peaks. The EDS measurement of the ordered mesoporous region for OMA-10Co was conducted and its profile was shown in Figure 3 (g). The characteristic peaks for Co, Al, and O elements could be clearly observed. This suggested that the Co element was successfully introduced into ordered mesoporous alumina matrix via the present one-step synthesis method.

The TEM characterizations of the as-reduced OMA-*x*Co catalysts were also investigated. The as-reduced OMA-3Co, OMA-5Co, and OMA-10Co catalysts were chosen as representatives and their TEM images were displayed in Figure S2 (ESI). The alignment of cylindrical pores along [1 1 0] direction for the as-reduced catalysts were successfully preserved after the reduction process under severe condition (800 ^{o}C for 2 h), demonstrating the excellent thermal stability. Furthermore, there was no evident agglomeration of metallic Co within the ordered mesoporous channels, indicating the high dispersion of metallic Co species within the whole mesoporous framework.

3.1.4. XPS analysis

XPS measurement was used to determine the chemical oxidation state of the surface Co species over as-synthesized OMA-*x*Co, NPA-10Co, and 10%Co/Al_2O_3. Their Co2p XPS profiles were shown in Figure 4. It was worth noting in Figure 4 (1) that all the as-prepared OMA-*x*Co samples presented similar peak shape profiles. Specifically, all the samples displayed an obvious $Co2p_{3/2}$ peak around 781.83 eV, a weak shake-up satellite peak around 786.86 eV, and a $Co2p_{1/2}$ peak around 798.40 eV, respectively. Compared with literatures reported $Co2p_{3/2}$ characteristic binding energy values for cobalt compounds, such as $Co(OH)_2$ (780.9 eV), Co_3O_4 (780.0 eV), $CoAl_2O_4$ (781.0 eV), etc [45, 47-49], the oxidation state of Co species in the present OMA-*x*Co was ascribed to Co^{2+} in the form of $CoAl_2O_4$ spinel, in good agreement with the XRD result in Figure 1 (2).

Figure 4 (2) presented the comparative analyses of Co2p XPS profiles for OMA-10Co, NPA-10Co, and 10%Co/Al_2O_3 catalysts with the same Co loading. As for the NPA-10Co, it exhibited similar patterns to OMA-10Co in the peak position and shape. This suggested that its surface Co species was also present in the form of $CoAl_2O_4$ spinel, as verified by XRD analysis in Figure 1. We proposed that during one-step synthesis process, the precursors of Co and Al species could mix thoroughly and react with each other sufficiently. As a result, Co species could enter into the bulk alumina matrix during the process of calcination, promoting the formation of $CoAl_2O_4$ spinel via the following process: $CoO + Al_2O_3 = CoAl_2O_4$. However, for the 10%Co/Al_2O_3 catalyst, its Co2p spectrum was quite different with OMA-10Co in both peak position and shape. Specifically, the $Co2p_{3/2}$ (780.33 eV) binding energy of 10%Co/Al_2O_3 was much lower than that of OMA-10Co (781.83 eV), which was attributable to Co_3O_4 species [45, 47, 49]. Additionally, there was no shake-up satellite peak accompanying the $Co2p_{3/2}$ peak for 10%Co/Al_2O_3, which was the typical feature for $CoAl_2O_4$ spinel species [48].

3.1.5. H_2-TPR analysis

In order to investigate the interaction between Co species and mesoporous framework, the H_2-TPR measurements of the as-synthesized OMA-*x*Co catalysts were carried out, as shown in

Figure 5 (1). The intensities of the H_2 reduction peaks gradually increased with the increase of Co containing for most of the samples, indicating the augment in H_2 consumption. It was also noteworthy that most of the samples presented similar hydrogen consumption profiles in the shape regardless of Co content, displaying one pronounced H_2 reduction peak in the region above 1080 ^oC and one broad shoulder peak in the region of 746–937 ^oC, respectively. There was no reduction peak observed in the range of 300-450 ^oC for all the mesoporous catalysts. This implied the absence of the free CoO and/or Co_3O_4 species that were not interacted with the mesoporous framework [43, 48, 50]. The XRD and XPS measurements discussed above confirmed the presence of $CoAl_2O_4$ spinel in the OMA-*x*Co framework. The $CoAl_2O_4$ spinel can only be reduced at high temperature due to the strong interaction between Co and the mesoporous framework [48, 51, 52]. Therefore, these two reduction peaks in different temperature regions should be ascribed to the reduction of Co^{2+} from +2 to 0 valence state, which were in different coordination environments. As for the reduction peaks in the region of 746-937 ^oC, they might be assigned to the reduction of surface Co species. On one hand, the unsaturated coordination of the surface Co^{2+} made them easier to reduce; on the other hand, the surface Co^{2+} could be more easily accessible to H_2 stream owing to their large surface areas and uniform pore channels. As a result, they could be reduced in relatively lower temperature region. The reduction peaks at higher temperature region above 1080 ^oC could be ascribed to the reduction of the saturated coordinated Co^{2+}, which has strong metal-support interaction with the mesoporous framework.

Furthermore, the comparative analysis of H_2-TPR profiles for OMA-10Co, NPA-10Co, and 10%Co/Al_2O_3 catalysts were summarized in Figure 5 (2). For the NPA-10Co catalyst, it presented obvious reduction peaks in high temperature region similar to OMA-10Co. It displayed high reduction peaks in high temperature regions, which were also attributed to the reduction of $CoAl_2O_4$ spinel species in different coordination environments. In addition, the little uptake peaks in low temperature region around 586 ^oC could be attributed to the reduction of Co oxides, which had weak interaction with the bulk catalyst. This might be caused by the absence of self-assembly step around P123 template during its synthesis process. As a result, the Co species could not be completely transformed into $CoAl_2O_4$ and parts of Co species existed in the state of cobalt oxides (CoO or/and Co_3O_4). In the case of the 10%Co/Al_2O_3 catalyst, its profile displayed three obvious reduction peaks centered around 607, 786, 989 ^oC, respectively, which could be attributed to the first step reduction of Co_3O_4 and subsequent reduction of CoO species. Because the XRD and XPS analyses had confirmed the presence of Co_3O_4 crystalline phase over 10%Co/Al_2O_3 supported catalyst. For the reduction peak at 607 ^oC, it could be derived from the first step reduction of Co_3O_4 (I) (Co_3O_4 (I) + H_2 = 3CoO (I) + H_2O), which had weak interaction with Al_2O_3 support. The peak centered at 786 ^oC, however, might be stemmed from both the subsequent reduction of CoO (I) (CoO (I) + H_2 = Co + H_2O) and first step reduction of Co_3O_4 (II) strongly interacted with the support. The last peak around 989 ^oC was attributed to the further reduction of CoO (II) derived from Co_3O_4 (II), which also had strong interaction with the Al_2O_3 support.

3.2. Catalytic performances

3.2.1. Effect of reaction temperature

In order to investigate the influence of the reaction temperature, the catalytic performances of CRM reaction over the OMA-*x*Co with different Co content at different temperatures under particular conditions (CH_4/CO_2 = 1, GHSV = 15000 mL/(g·h), 1 atm) were summarized in Figure 6 (1) and (2). The conversions of CH_4 and CO_2 were greatly promoted with the increase of the reaction temperature. Typically, they displayed the highest activity at 800 ^oC in the present temperature region investigated regardless of the Co containing due to the intensively endothermic nature of the CRM reaction [12]. The relationship between the catalytic activity and Co content for OMA-*x*Co catalysts was also studied. With the augment of the Co content, the conversions of CH_4 and CO_2 rapidly increased in the initial stage and reached the maximum value at 10% Co containing for all the temperature stages. This could be attributed to the increasing number of Co active sites to provide the gaseous feedstock with more accessible metallic active sites under similar reduction conditions. However, higher content of Co up to 15% caused sharp drop in CH_4 and CO_2 conversion, arising from the thermal agglomeration of the Co active centers and hence the decrease of active sites.

3.2.2. Effect of gas hourly space velocity (GHSV)

The influence of gas hourly space velocity (GHSV) on the conversions of CH_4 and CO_2 was equally investigated under given conditions (CH_4/CH_4 = 1, 750 ^oC, 1 atm) over OMA-*x*Co catalysts. As shown in the Figure 6 (3) and (4), with the increase of feed flow from 7200 to 45000 mL/(g·h), the conversions of CH_4 and CO_2 rapidly decreased (e.g. decreased from 88.9% to 60.5% for the CH_4 conversion over OMA-10Co) over all the catalysts investigated. It had been proposed that the reduction in the residence time of the reactants on the catalyst surface and the drop in catalyst bed temperature could result in these phenomena [53]. However, as for the present OMA-*x*Co catalysts, we proposed that the decrease in the residence time over catalyst surface and the limited active sites for the increasing reactants were the main reasons. With the increase of the GHSV, the velocity for the gaseous reactants through the catalyst bed became faster and residence time over the catalyst bed became shorter. However, as the GHSV increased, the number of the reactants through the catalyst bed largely increased, making active sites nonsufficient for redundant reactants. The effect of the Co containing on the catalytic activity for OMA-*x*Co catalysts under different GHSV could also be learned. For the OMA-*x*Co catalysts under given GHSV, the OMA-10Co still possessed the highest CH_4 and CO_2 conversion among all the catalysts studied. It was of great interest to observe that the OMA-10Co always displayed the best catalytic activity among the OMA-*x*Co catalysts under different GHSV investigated, same as the conditions at different temperatures.

3.2.3. Effect of ordered mesostructure

In order to investigate the role of the ordered mesoporous framework in promoting CRM catalytic activity, the comparative analyses of OMA-10Co, NPA-10Co, and 10%Co/Al_2O_3 catalysts with identical Co containing were systematically carried out under different reaction conditions. As shown in Figure 7, the CH_4, CO_2 conversions for OMA-10Co mesoporous catalyst were much higher than those for NPA-10Co and 10%Co/Al_2O_3 catalysts under different reaction conditions. This demonstrated that the ordered mesostructure could significantly promote the catalytic activity. Compared with NPA-10Co without obvious mesoporous structure, the mesoporous catalyst possessed larger surface area, bigger pore volume, and more barrier-free pore channels. By contrast, most of the Co species were located in the bulk of the material for NPA-10Co. Therefore, the mesoporous catalysts could provide much more exposed Co active centers for the gaseous reactants, which accounted for the higher catalytic activity of OMA-10Co than that of NPA-10Co. As for the 10%Co/Al_2O_3 supported catalyst, the severe thermal agglomeration of the metallic Co active sites was prone to take place during the processes of catalyst reduction and CRM reaction due to the weak interaction between metal and support. At this point, the OMA-10Co catalyst presented better performance than 10%Co/Al_2O_3. The Co species could be effectively confined by the mesoporous framework due to the advantage of one-step synthesis strategy, which would effectively stabilize the Co metallic active sites under severe reduction and CRM reaction conditions. Therefore, the decrease in the number of Co active centers caused by thermal sintering could be effectively avoided to some degree, which accounted for the higher catalytic activity than 10%Co/Al_2O_3.

3.2.4. Long-term stability tests of the catalysts

Laboratory-scale 60 h long-term stability tests over OMA-10Co, OMA-7Co, NPA-10Co, and 10%Co/Al_2O_3 catalysts were performed respectively under specific reaction conditions: 750 ^{o}C, GHSV = 15000 mL/(g·h), CH_4/CO_2 = 1, 1 atm. As shown in Figure 8, OMA-10Co and OMA-7Co catalysts with ordered mesostructures performed both high catalytic activities and excellent catalytic stabilities during the whole 60 h test; on the contrary, NPA-10Co and 10%Co/Al_2O_3 samples suffered gradual decline in CH_4 and CO_2 conversions (e.g. from 79.9% to 50.6% for CH_4 conversion over NPA-10Co). It was well known that developing catalyst with enhanced stability was significant for future large-scale industrialization of CRM process. Previous studies had revealed that the metallic active center with smaller size possessed strengthened capacity of coke suppression, also known as size effect [33, 34]. For the OMA-10Co and OMA-7Co catalysts, the growth of the Co particles was effectively suppressed by the confinement effect of the mesoporous framework during the processes of catalyst reduction and CRM reaction, thereby leading to good catalytic stability. For NPA-10Co, the absence of ordered mesostructure could cause the thermal sintering of the metallic active centers. At the same time, due to the weak interaction between metal and support, the thermal agglomeration of the Co species could take place on the 10%Co/Al_2O_3 supported catalyst, thereby leading to the gradually continuous deactivation. The metallic clusters with large sizes facilitated the methane decomposition and carbon deposition, hence resulting in the rapid deactivation of the catalyst and large amount of surface coke [33, 34]. For the H_2/CO ratios over these catalysts, they were all less than 1, as shown in Figure 8 (3). This was derived from reverse water gas shift side reaction (RWGS, $CO_2(g) + H_2(g) = H_2O(g) + CO(g)$, ΔH_{298}= +41 kJ/mol), which could consume H_2 and generate CO [12]. The H_2/CO ratios over OMA-10Co and OMA-7Co mesoporous catalysts were constant around 0.87 and 0.83, respectively, indicating that the equilibrium between the coke deposition reaction and elimination reaction had been achieved [53, 54]. As a comparison, the H_2/CO ratio for NPA-10Co sample decreased continuously from 0.99 to 0.76, implying that the balance between carbon deposition and coke elimination could not be finally achieved. The rate of carbon deposition reaction was much faster than that of coke elimination reaction. Therefore, the coke deposition over the catalyst surface was very serious and the catalyst subsequently suffered quick deactivation.

3.3. Characterization of the spent catalysts

3.4.1. TG analysis

In view of the carbon balance, most carbon atoms of the feed gases (CH_4, CO_2) were converted into the final product in the form of CO. However, there was also part of the carbon atoms deposited on the surface of the catalyst in the form of the coke due to the presence of side reactions under CRM reaction condition, such as methane decomposition, Boudouard reaction, etc. Therefore, the properties of the carbon deposition over the OMA-7Co, OMA-10Co, NPA-10Co, and 10%Co/Al_2O_3 catalysts after 60 h long-term stability test were examined by TG analysis. As shown in Figure 9. The weight losses over OMA-7Co, OMA-10Co, 10%Co/Al_2O_3, and NPA-10Co catalysts were 6.7%, 10.0%, 16.0%, and 43.5%, respectively. In contrast with 10%Co/Al_2O_3 and NPA-10Co catalysts, OMA-7Co and OMA-10Co mesoporous catalysts possessed much less carbon deposition and hence better anti-coke performance. The mesoporous framework could stabilize the Co particles in nano-size during the processes of reduction and CRM reaction via its confinement effect, thereby significantly suppressing the coke formation owing to the size effect of metallic active sites.

3.4.2. TPH analysis

TPH technique could be used to study the types of the coke deposited on the catalyst. The coke of different types possessed different hydrogenation performances to generate CH_4. Generally, the coke with high activity usually presented CH_4 signal peak at low temperature region; on the contrary, the species with low activity exhibited CH_4 signal peak at high temperature region [55-57]. TPH characterization was carried out over 60 h endurance-tested OMA-7Co, OMA-10Co, NPA-10Co, and 10%Co/Al_2O_3 catalysts to study the characteristics of the surface coke species and their profiles were shown in Figure 10. Most of the samples displayed CH_4 signal peaks with similar shapes, with one weak peak around 400 ^oC and one strong peak around 640 ^oC (or even higher temperature around 750 ^oC), respectively, which could be assigned to two kinds of carbon deposition with different reactivity toward hydrogenation. The weak shoulder peaks around 400 ^oC was proposed to arise from the hydrogenation of amorphous carbon deposition [55-58], which was responsible for the CO formation during the reaction [10, 55, 56, 59, 60]. The main peaks around 640 ^oC could be attributable to the hydrogenation peak of carbon nanotube species, which had much lower reactivity toward H_2 hydrogenation than the amorphous carbon and finally caused the deactivation of the catalyst by covering metallic active sites and blocking pore channels [56, 58, 61].

3.4.3. Morphology analysis of the long-term endurance-tested catalysts

TEM analysis of the 60 h endurance-tested OMA-10Co, OMA-7Co, NPA-10Co, and 10%Co/Al_2O_3 catalysts was performed to further confirm the thermal stability of the ordered mesostructure and investigate the morphology of carbon deposition over catalyst surface, as shown in Figure 11. The OMA-7Co and OMA-10Co ordered mesoporous catalysts could well retain the uniform cylindrical mesopores along [1 1 0] direction and the hexagonal honeycomb-like mesopores along [0 0 1] direction even after 60 h long time CRM reaction, in good agreement with their IV H1 hysteresis loops and narrow pore size distributions in Figure S3 (ESI). This suggested that these ordered mesoporous catalysts possessed good thermal stability. It was worth noting that there was no obvious large and aggregated Co metallic cluster observed over these mesoporous catalysts. This further confirmed that the confinement effect of the mesoporous framework played an important role in stabilizing Co metallic nanoparticles during the long-term stability test. In addition, the carbon nanotube was the main coke residue for all the catalysts studied, as predicted by the TPH characterization, which would cause the rapid deactivation of the catalysts [61, 62]. In contrast, there was no apparent amorphous carbon species found among the catalysts. We proposed that the amorphous carbon might uniformly distribute among the mesoporous channels and catalyst surface, which could be further eliminated in the subsequent process of CO production.

4. Conclusion

In conclusion, a series of ordered mesoporous $CoAl_2O_4$ spinel based metal oxides with different Co content were firstly designed and facilely prepared by one-step evaporation induced self-assemble method. The obtained materials with excellent structural property and good thermal stability were utilized as the catalysts for the CRM reaction. Compared with non-mesoporous and traditional supported catalysts, these mesoporous catalysts performed higher catalytic activity and better stability. The ordered mesoporous structure could significantly improve catalytic activity and stability, by providing sufficient accessible Co metallic active sites for the gaseous feed stocks and stabilizing the Co nanoparticles via the confinement effect of the mesoporous framework during the CRM reaction, simultaneously. In addition, the OMA-*x*Co catalysts had strong capacity of coke resistance due to the size effect of the Co nanoparticles. Our results demonstrated that these OMA-*x*Co materials could be considered as a series of promising catalysts for the CRM reaction.

Acknowledgements

The authors acknowledge the financial support from Singapore MOE grant R143-000-542-112, Singapore National Research Foundation CREATE-SPURc program R-143-001-205-592, and Jiangsu Province Government Research Platform Grant and NUSRI Seed Fund.

References

1. A. Baiker, *Appl. Organomet. Chem.*, 2000, 14, 751-762.

2. I. Omae, *Catal. Today*, 2006, 115, 33-52.

3.K. Mette, S. Kuehl, H. Duedder, K. Kaehler, A. Tarasov, M. Muhler and M. Behrens, *Chemcatchem*, 2014, 6, 100-104.

4. C. S. Song, *Catal. Today*, 2006, 115, 2-32.

5. W. Wang, S. Wang, X. Ma and J. Gong, *Chem. Soc. Rev.*, 2011, 40, 3703-3727.

6. R. Schloegl, *Chemsuschem*, 2010, 3, 209-222.

7. A. T. Ashcroft, A. K. Cheetham, M. L. H. Green and P. D. F. Vernon, *Nature*, 1991, 352, 225-226.

8. W. Chen, G. Zhao, Q. Xue, L. Chen and Y. Lu, *Appl. Catal. B: Environ.*, 2013, 136, 260-268.

9. Z. Liu, J. Zhou, K. Cao, W. Yang, H. Gao, Y. Wang and H. Li, *Appl. Catal. B: Environ.*, 2012,

125, 324-330.

10. M. Yu, K. Zhu, Z. Liu, H. Xiao, W. Deng and X. Zhou, *Appl. Catal. B: Environ.*, 2014, 148, 177-190.

11. S. Zeng, X. Zhang, X. Fu, L. Zhang, H. Su and H. Pan, *Appl. Catal. B: Environ.*, 2013, 136, 308-316.

12. M. C. J. Bradford and M. A. Vannice, *Cat. Revi.-Sci. Eng.*, 1999, 41, 1-42.

13. M.S. Fan, A. Z. Abdullah and S. Bhatia, *Chemcatchem*, 2009, 1, 192-208.

14. C.J. Liu, J. Ye, J. Jiang and Y. Pan, *Chemcatchem*, 2011, 3, 529-541.

15. B. Q. Xu and W. M. H. Sachtler, *J. Catal.*, 1998, 180, 194-206.

16. J. R. H. Ross, A. N. J. vanKeulen, M. E. S. Hegarty and K. Seshan, *Catal. Today*, 1996, 30, 193-199.

17. Y. H. Hu and E. Ruckenstein, *Catalysis Rev.-Sci. Eng.*, 2002, 44, 423-453.

18. N. Sun, X. Wen, F. Wang, W. Wei and Y. Sun, *Energy Environ. Sci.*, 2010, 3, 366-369.

19. K. Takanabe, K. Nagaoka, K. Nariai and K. Aika, *J. Catal.*, 2005, 232, 268-275.

20. S. Liu, L. Guan, J. Li, N. Zhao, W. Wei and Y. Sun, *Fuel*, 2008, 87, 2477-2481.

21. P. Ferreira-Aparicio, A. Guerrero-Ruiz and I. Rodriguez-Ramos, *Appl. Catal. A: Gen.*, 1998, 170, 177-187.

22. J. H. Edwards and A. M. Maitra, *Fuel Process. Technol.*, 1995, 42, 269-289.

23. A. W. Budiman, S.H. Song, T.S. Chang, C.H. Shin and M.J. Choi, *Catal. Surv. Asia*, 2012, 16, 183-197.

24. C. Shi and P. Zhang, *Appl. Catal. B: Environ.*, 2012, 115, 190-200.

25. X.Y. Quek, D. Liu, W. N. E. Cheo, H. Wang, Y. Chen and Y. Yang, *Appl. Catal. B: Environ.*, 2010, 95, 374-382.

26. M.S. Fan, A. Z. Abdullah and S. Bhatia, *Appl. Catal. B: Environ.*, 2010, 100, 365-377.

27. J. Zhang, H. Wang and A. K. Dalai, *J. Catal.*, 2007, 249, 300-310.

28. P. Djinovic, I. G. O. Crnivec, B. Erjavec and A. Pintar, *Appl. Catal. B: Environ.*, 2012, 125, 259-270.

29. E. Ruckenstein and H. Y. Wang, *Appl. Catal. A: Gen.*, 2000, 204, 257-263.

30. E. Ruckenstein and H. Y. Wang, *J. Catal.*, 2002, 205, 289-293.

31. N. Wang, W. Chu, L. Huang and T. Zhang, *J. Nat. Gas Chem.*, 2010, 19, 117-122.

32. S. B. Wang, G. Q. M. Lu and G. J. Millar, *Energy Fuels*, 1996, 10, 896-904.

33. J. H. Kim, D. J. Suh, T. J. Park and K. L. Kim, *Appl. Catal. A: Gen.*, 2000, 197, 191-200.

34. H. Y. Wang and E. Ruckenstein, *Appl. Catal. A: Gen.*, 2001, 209, 207-215.

35. W. Zhu, A. Borjesson and K. Bolton, *Carbon*, 2010, 48, 470-478.

36. Y. H. Hu, *Catal. Today*, 2009, 148, 206-211.

37. K. Bourikas, C. Kordulis and A. Lycourghiotis, *Cat. Rev.-Sci. Eng.*, 2006, 48, 363-444.

38. S. Damyanova, B. Pawelec, K. Arishtirova, J. L. G. Fierro, C. Sener and T. Dogu, *Appl. Catal. B: Environ.*, 2009, 92, 250-261.

39. L. Y. Mo, J. H. Fei, C. J. Huang and X. M. Zheng, *J. Mol. Catal. A: Chem.*, 2003, 193, 177-184.

40. L. Y. Mo, X. M. Zheng, C. J. Huang and J. H. Fei, *Catal. Lett.*, 2002, 80, 165-169.

41. Q. Yuan, A.X. Yin, C. Luo, L.D. Sun, Y.W. Zhang, W.T. Duan, H.C. Liu and C.H. Yan, *J. Am. Chem. Soc.*, 2008, 130, 3465-3472.

42. S. M. Morris, P. F. Fulvio and M. Jaroniec, *J. Am. Chem. Soc.*, 2008, 130, 15210-15216.

43. H. Y. Wang and E. Ruckenstein, *Catal. Lett.*, 2001, 75, 13-18.

44. R. Liu, M. Yang, C. Huang, W. Weng and H. Wan, *Chin. J. Catal.*, 2013, 34, 146-151.

45. N. Srisawad, W. Chaitree, O. Mekasuwandumrong, P. Praserthdam and J. Panpranot, *J. Nanomater.*, 2012, 2012, 95.

46. L. Ji, J. Lin and H. C. Zeng, *J. Phys. Chem. B*, 2000, 104, 1783-1790.

47. R. L. Chin and D. M. Hercules, *The J. Phys. Chem.*, 1982, 86, 360-367.

48. H. Xiong, Y. Zhang, K. Liew and J. Li, *J. Mol. Catal. A: Chem.*, 2005, 231, 145-151.

49. Z. Ferencz, K. Baán, A. Oszkó, Z. Kónya, T. Kecskés and A. Erdőhelyi, *Catal. Today*, 2014, 228, 123-130.

50. H. F. Xiong, Y. H. Zhang, J. L. Li and Y. Y. Gu, *J. Cent. South Univ. Technol.*, 2004, 11, 414-418.

51. L. Ji, S. Tang, H. C. Zeng, J. Lin and K. L. Tan, *Appli. Catal. A: Gen.*, 2001, 207, 247-255.

52. J. L. Li, X. D. Zhan, Y. Q. Zhang, G. Jacobs, T. Das and B. H. Davis, *Appli. Catal. A: Gen.*, 2002, 228, 203-212.

53. J. M. Wei, B. Q. Xu, J. L. Li, Z. X. Cheng and Q. M. Zhu, *Appli. Catal. A: Gen.*, 2000, 196, L167-L172.

54. L. Xu, H. Song and L. Chou, *Catal. Sci. Technol.*, 2011, 1, 1032-1042.

55. L. Xu, H. Song and L. Chou, *Appl. Catal. B: Environ.*, 2011, 108, 177-190.

56. M. Rezaei, S. M. Alavi, S. Sahebdelfar, P. Bai, X. Liu and Z.-F. Yan, *Appl. Catal. B: Environ.*, 2008, 77, 346-354.

57. M. Rezaei, S. M. Alavi, S. Sahebdelfar and Z.-F. Yan, *J. Nat. Gas Chem.*, 2008, 17, 278-282.

58. J. Guo, H. Lou and X. Zheng, *Carbon*, 2007, 45, 1314-1321.

59. H. M. Swaan, V. C. H. Kroll, G. A. Martin and C. Mirodatos, *Catal. Today*, 1994, 21, 571-578.

60. Y. G. Chen and J. Ren, *Catal. Letters*, 1994, 29, 39-48.

61. C. Wang, N. Sun, N. Zhao, W. Wei, J. Zhang, T. Zhao, Y. Sun, C. Sun, H. Liu and C. E. Snape, *ChemCatChem*, 2014, 6, 640-648.

62. H. Liu, C. Guan, X. Li, L. Cheng, J. Zhao, N. Xue and W. Ding, *ChemCatChem*, 2013, 5, 3904-3909.

Figure and table captions:

Table 1

Structural properties of the as-synthesized, as-reduced, and 60 h endurance-tested catalysts.

Figure 1

(1) Small-angle and **(2)** Wide-angle XRD patterns of the as-synthesized OMA-*x*Co catalysts: **(a)** OMA-3Co, **(b)** OMA-5Co, **(c)** OMA-7Co, **(d)** OMA-10Co, **(e)** OMA-15Co;

(3) XRD patterns of the as-synthesized and **(4)** as-reduced catalysts prepared by different methods: **(a)** OMA-10Co, **(b)** NPA-10Co, **(c)** 10%Co/Al_2O_3.

Figure 2

Nitrogen adsorption-desorption isotherms (**(1), (3)**) and pore size distribution curves (**(2), (4)**) of the as-synthesized catalysts.

Figure 3

TEM, SAED, and EDS measurements of the as-synthesized OMA-*x*Co catalysts: **(a)** OMA-3Co, **(b)** and **(c)** OMA-5Co, **(d)** OMA-7Co, **(e)** and **(g)** OMA-10Co, **(f)** OMA-15Co.

Figure 4

(1) XPS profiles of Co2p for the as-synthesized OMA-*x*Co catalysts: **(a)** OMA-3Co, **(b)** OMA-5Co, **(c)** OMA-7Co, **(d)** OMA-10Co, **(e)** OMA-15Co;

(2) XPS profiles of Co2p for the as-synthesized catalysts prepared by different methods: **(a)** OMA-10Co, **(b)** NPA-10Co, **(c)** 10%Co/Al_2O_3.

Figure 5

(1) H_2-TPR profiles of the OMA-*x*Co catalysts: **(a)** OMA-3Co, **(b)** OMA-5Co, **(c)** OMA-7Co, **(d)** OMA-10Co, **(e)** OMA-15Co;

(2) H_2-TPR profiles of the catalysts prepared by different methods: **(a)** OMA-10Co, **(b)** NPA-10Co, **(c)** 10%Co/Al_2O_3.

Figure 6

(I) The curves of the **(1)** CH_4 conversion and **(2)** CO_2 conversion versus reaction temperature for OMA-*x*Co catalysts with different Co content; reaction conditions: $CH_4/CO_2 = 1$, GHSV = 15000 mL/(g.h), 1 atm.

(II) The curves of the **(3)** CH_4 conversion and **(4)** CO_2 conversion versus gas hourly space velocity (GHSV) for OMA-*x*Co catalysts with different Co content; reaction conditions: $CH_4/CO_2 = 1$, 750

^{o}C, 1 atm.

Figure 7

(I) The curves of the **(1)** CH_4 conversion and **(2)** CO_2 conversion versus reaction temperature for catalysts prepared with different methods; reaction conditions: CH_4/CO_2 = 1, GHSV = 15000 mL/(g.h), 1 atm.

(II) The curves of the **(3)** CH_4 conversion and **(4)** CO_2 conversion versus gas hourly space velocity (GHSV) for catalysts prepared with different methods; reaction conditions: CH_4/CO_2 = 1, 750 ^{o}C, 1 atm.

Figure 8

60 h long-term stability tests over different catalysts; reaction conditions: CH_4/CO_2 = 1, GHSV = 15000 mL/(g.h), 750 ^{o}C, 1 atm.

Figure 9

TG curves of the 60 h endurance-tested catalysts: **(a)** OMA-7Co, **(b)** OMA-10Co, **(c)** NPA-10Co, **(d)** 10%Co/Al_2O_3.

Figure 10

TPH profiles of the 60 h endurance-testd catalysts: **(a)** OMA-7Co, **(b)** OMA-10Co, **(c)** NPA-10Co, **(d)** 10%Co/Al_2O_3.

Figure 11

TEM images of the 60 h endurance-tested catalysts: **(a)**, **(b)**, and **(c)** OMA-7Co, **(d)**, **(e)**, and **(f)** OMA-10Co, **(g)** NPA-10Co, **(h)** and **(i)** 10%Co/Al_2O_3.

Table 1

Samples	Specific Surface Area (m^2/g)	Pore Volume (cm^3/g)	Average Pore Diameter (nm)	Isotherm Type
OMA-3Co	148.4	0.28	9.9	IV H1
OMA-5Co	196.5	0.27	9.8	IV H1
OMA-7Co	152.5	0.24	9.8	IV H1
OMA-10Co	207.6	0.31	9.8	IV H1
10Co/Al_2O_3	99.3	0.17	6.0	IV H3
NPA-10Co	85.6	0.08	—	IV H3
OMA-15Co	150.4	0.25	12.8	IV H1
AR[a]- OMA-3Co	107.7	0.27	9.8	IV H1
AR-OMA-5Co	124.1	0.28	9.8	IV H1
AR-OMA-7Co	87.2	0.19	9.9	IV H1
AR-OMA-10Co	133.8	0.25	9.9	IV H1
AR-10Co/Al_2O_3	96.9	0.18	6.7	IV H3
AR-NPA-10Co	77.5	0.05	—	IV H3
AR-OMA-15Co	89.2	0.19	12.6	IV H1
SP-OMA-7Co	125.6	0.18	8.1	IV H1
SP[b]-OMA-10Co	119.8	0.15	8.0	IV H1
SP-10Co/Al_2O_3	89.2	0.16	4.3	IV H3
SP-NPA-10Co	61.4	0.09	—	IV H3

a. AR stands for the meaning of "as-reduced";

b. SP stands for the meaning of "60 h spent".

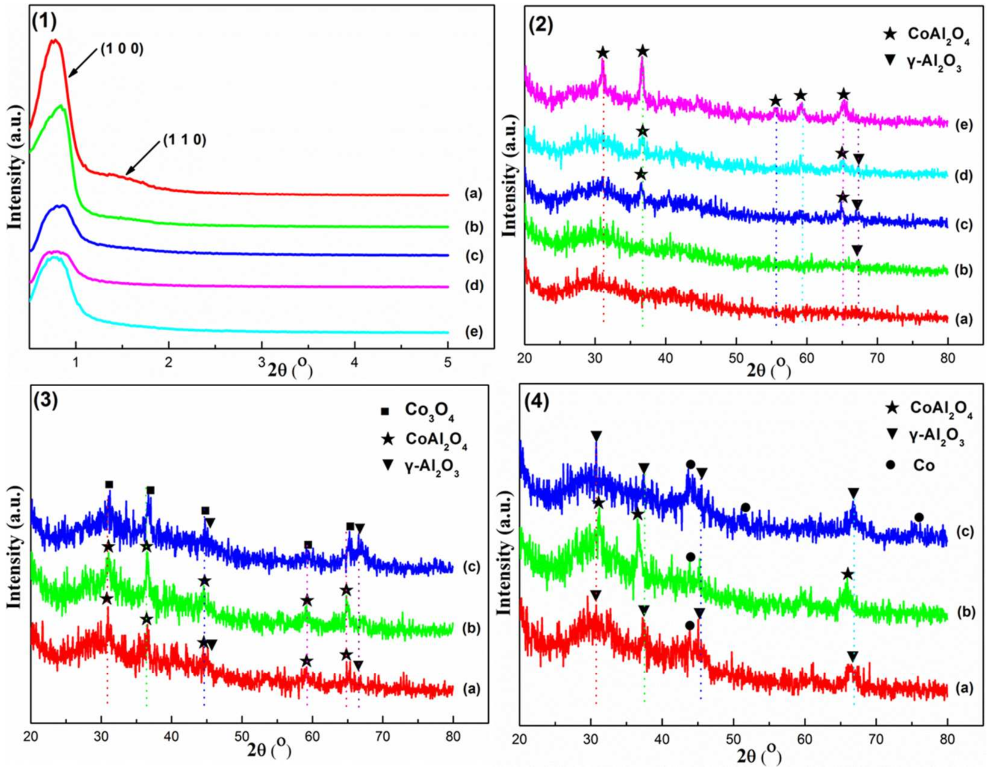
(1)
(1 0 0)
(1 1 0)
Intensity (a.u.)
(a)
(b)
(c)
(d)
(e)
1
2
3
4
5
2θ (°)
(2)
★ CoAl2O4
▼ γ-Al2O3
(e)
(d)
(c)
(b)
(a)
20
30
40
50
60
70
80
2θ (°)
(3)
■ Co3O4
★ CoAl2O4
▼ γ-Al2O3
(c)
(b)
(a)
(4)
★ CoAl2O4
▼ γ-Al2O3
● Co
(c)
(b)
(a)

Figure 1

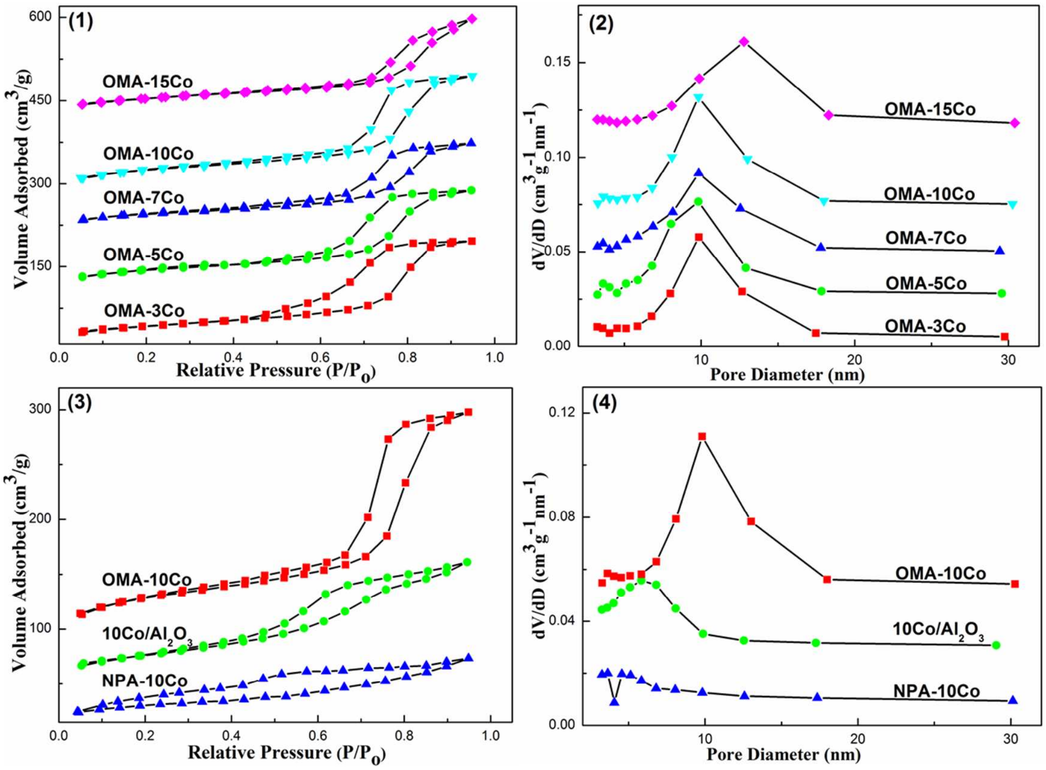
(1)
OMA-15Co
OMA-10Co
OMA-7Co
OMA-5Co
OMA-3Co
Volume Adsorbed (cm^3/g)
600
450
300
150
0.0
0.2
0.4
0.6
0.8
1.0
Relative Pressure (P/P$_0$)
(2)
OMA-15Co
OMA-10Co
OMA-7Co
OMA-5Co
OMA-3Co
dV/dD (cm^{3}g^{-1}nm^{-1})
0.15
0.10
0.05
0.00
10
20
30
Pore Diameter (nm)
(3)
OMA-10Co
10Co/Al$_2$O$_3$
NPA-10Co
Volume Adsorbed (cm^3/g)
300
200
100
0.0
0.2
0.4
0.6
0.8
1.0
Relative Pressure (P/P$_0$)
(4)
OMA-10Co
10Co/Al$_2$O$_3$
NPA-10Co
dV/dD (cm^{3}g^{-1}nm^{-1})
0.12
0.08
0.04
0.00
10
20
30
Pore Diameter (nm)

Figure 2

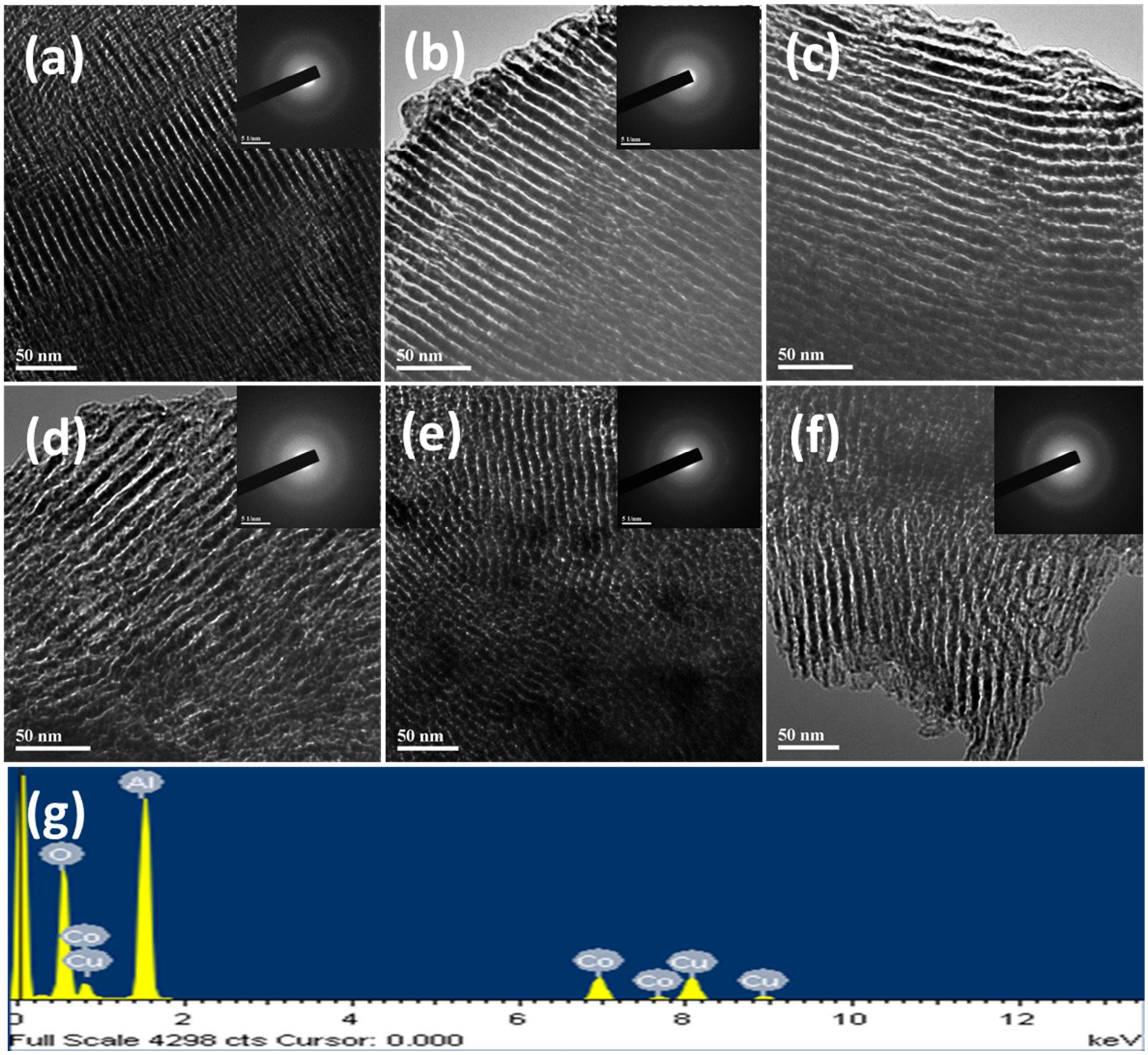
(a)
(b)
(c)
(d)
(e)
(f)
(g)
50 nm
5 1/nm
Al
O
Co
Cu
Co
Co
Cu
Cu
0
2
4
6
8
10
12
Full Scale 4298 cts Cursor: 0.000
keV

Figure 3

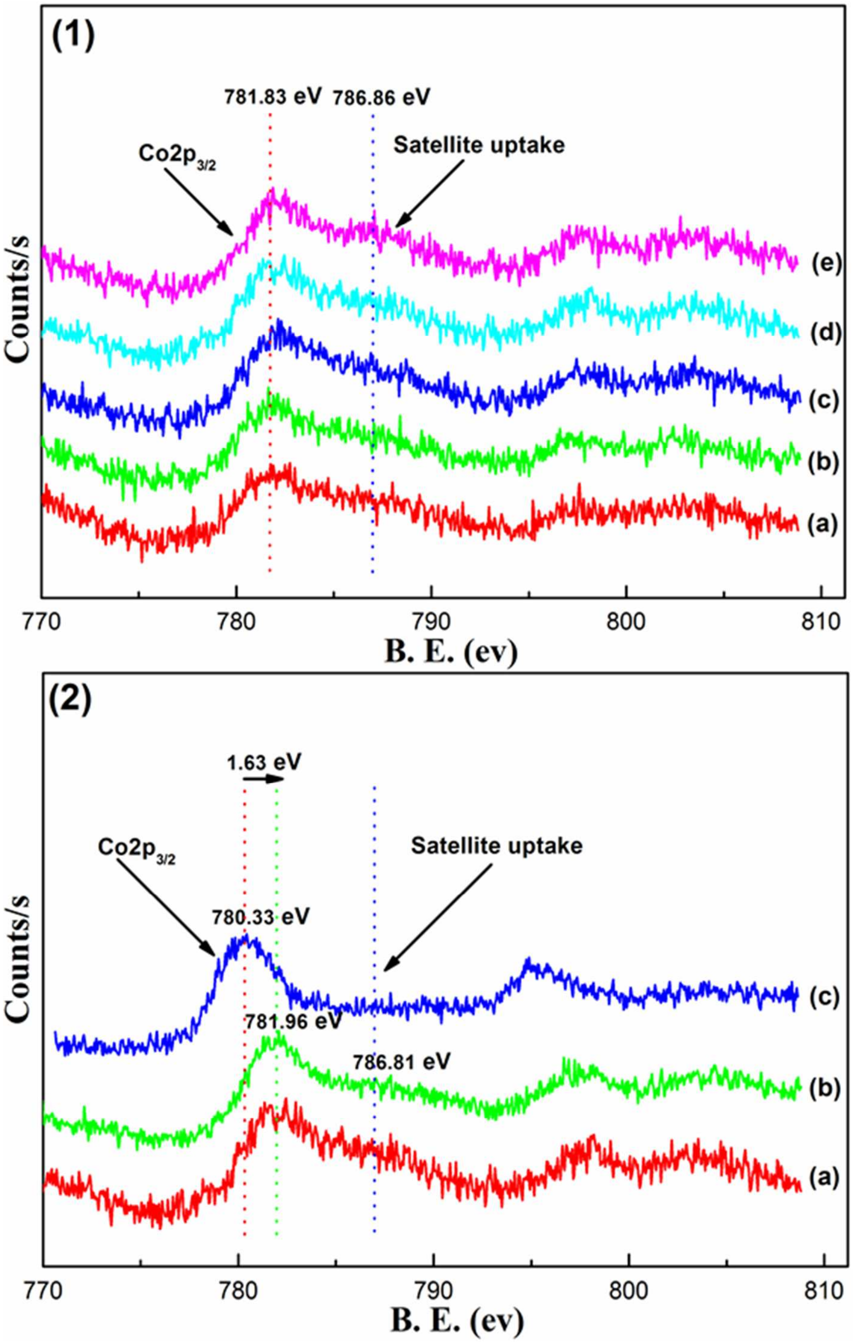
(1)
781.83 eV
786.86 eV
Co2p$_{3/2}$
Satellite uptake
(e)
(d)
(c)
(b)
(a)
Counts/s
770
780
790
800
810
B. E. (ev)
(2)
1.63 eV
Co2p$_{3/2}$
Satellite uptake
780.33 eV
781.96 eV
786.81 eV
(c)
(b)
(a)
Counts/s
770
780
790
800
810
B. E. (ev)

Figure 4

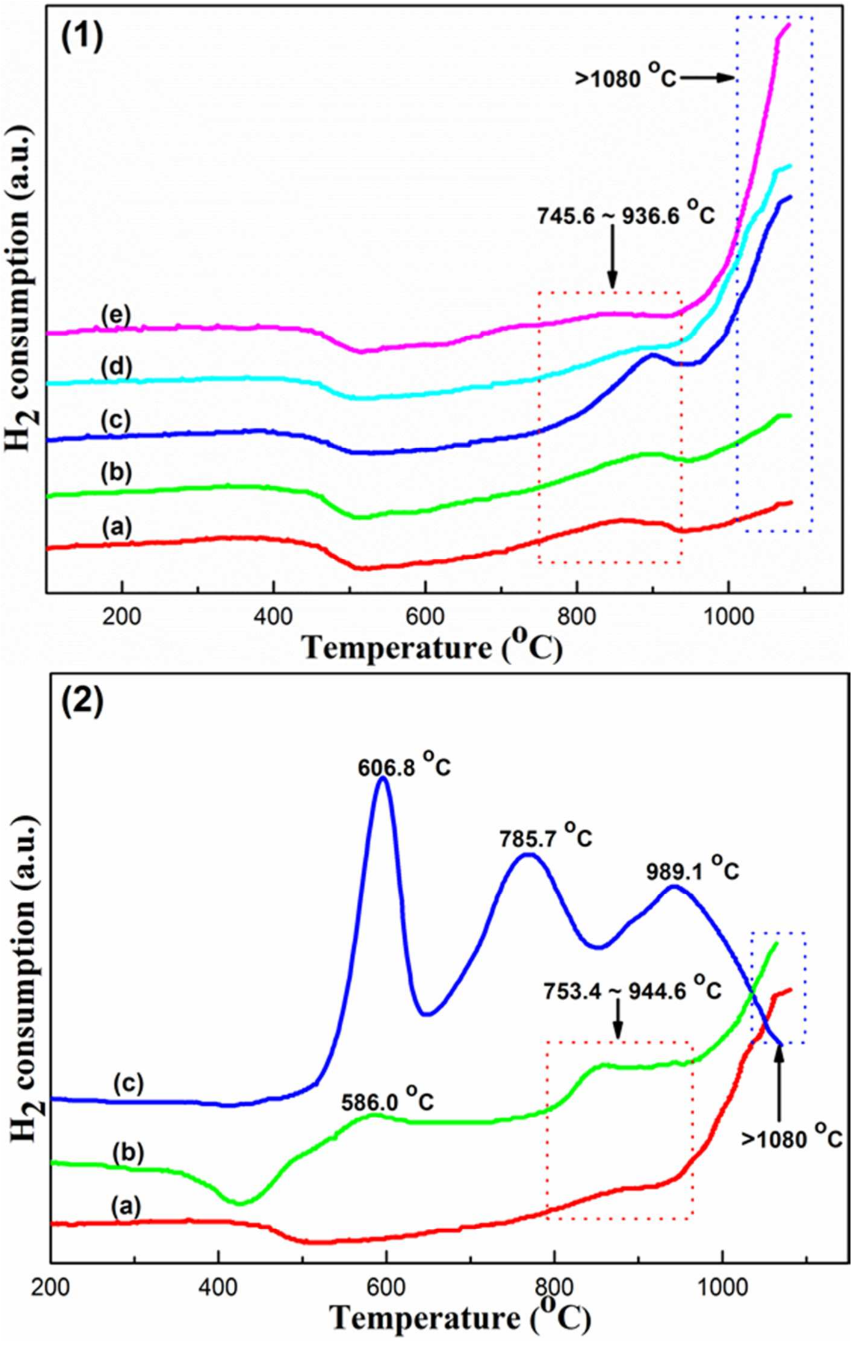
(1)
>1080 °C
745.6 ~ 936.6 °C
(e)
(d)
(c)
(b)
(a)
H2 consumption (a.u.)
200
400
600
800
1000
Temperature (°C)
(2)
606.8 °C
785.7 °C
989.1 °C
753.4 ~ 944.6 °C
586.0 °C
(c)
(b)
(a)
>1080 °C
H2 consumption (a.u.)
200
400
600
800
1000
Temperature (°C)

Figure 5

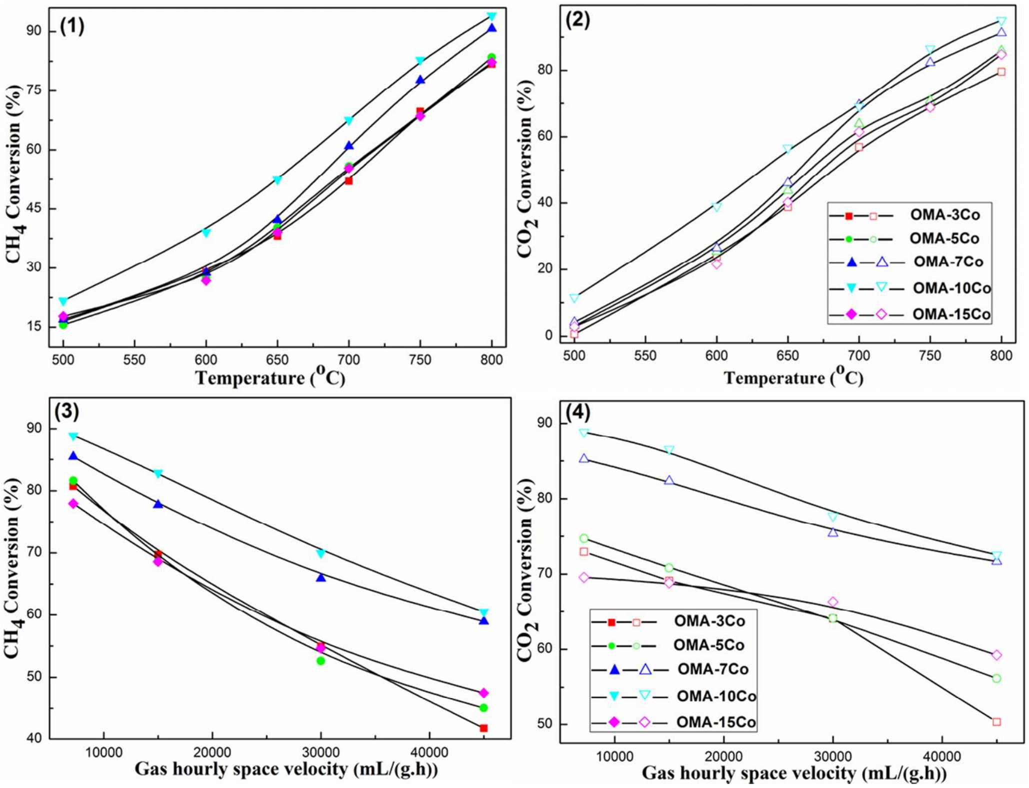
(1)
CH4 Conversion (%)
Temperature (°C)
(2)
CO2 Conversion (%)
Temperature (°C)
(3)
CH4 Conversion (%)
Gas hourly space velocity (mL/(g.h))
(4)
CO2 Conversion (%)
Gas hourly space velocity (mL/(g.h))
OMA-3Co
OMA-5Co
OMA-7Co
OMA-10Co
OMA-15Co

Figure 6

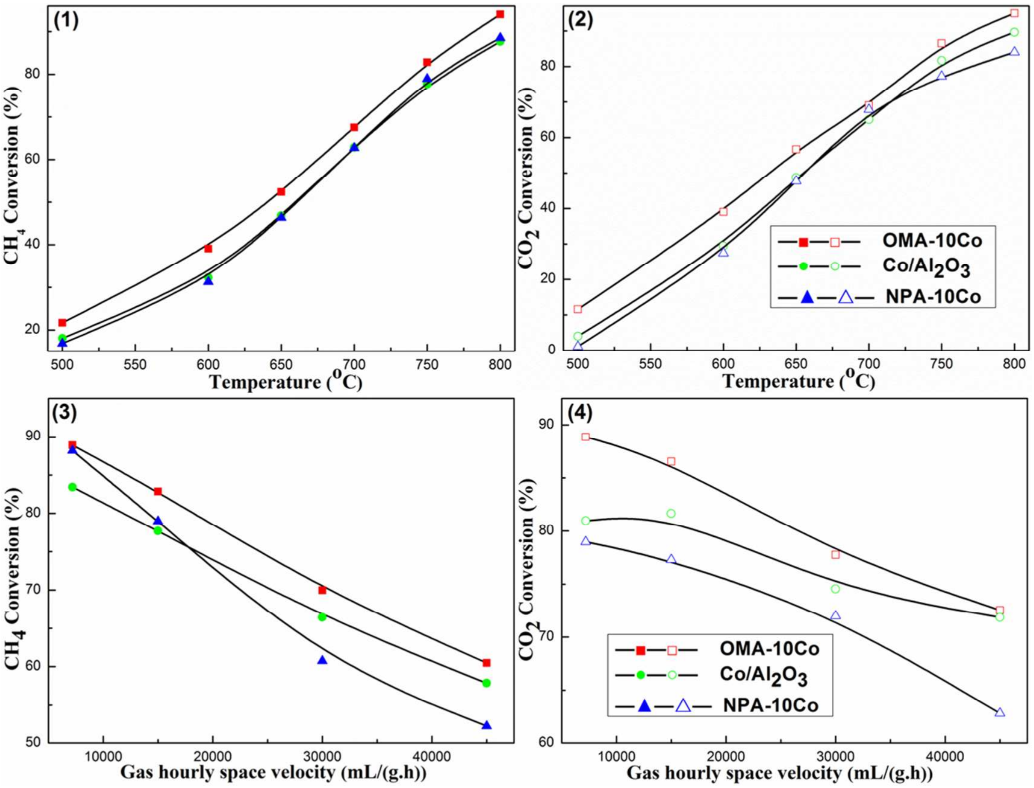
(1)
CH4 Conversion (%)
20
40
60
80
500
550
600
650
700
750
800
Temperature (°C)
(2)
CO2 Conversion (%)
0
20
40
60
80
OMA-10Co
Co/Al2O3
NPA-10Co
(3)
CH4 Conversion (%)
50
60
70
80
90
10000
20000
30000
40000
Gas hourly space velocity (mL/(g.h))
(4)
CO2 Conversion (%)
60
70
80
90

Figure 7

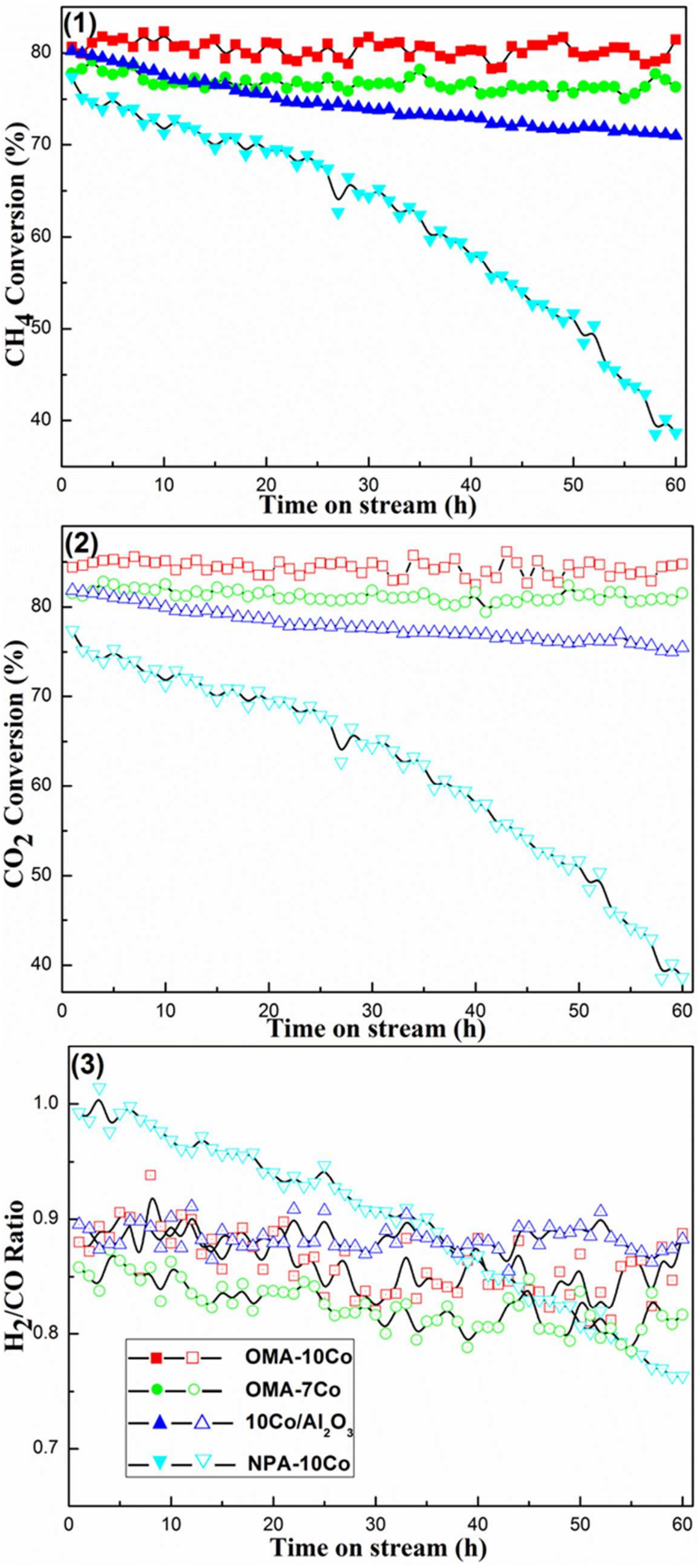
(1)
CH_4 Conversion (%)
80
70
60
50
40
0
10
20
30
40
50
60
Time on stream (h)
(2)
CO_2 Conversion (%)
80
70
60
50
40
0
10
20
30
40
50
60
Time on stream (h)
(3)
H_2/CO Ratio
1.0
0.9
0.8
0.7
0
10
20
30
40
50
60
Time on stream (h)
OMA-10Co
OMA-7Co
10Co/Al_2O_3
NPA-10Co

Figure 8

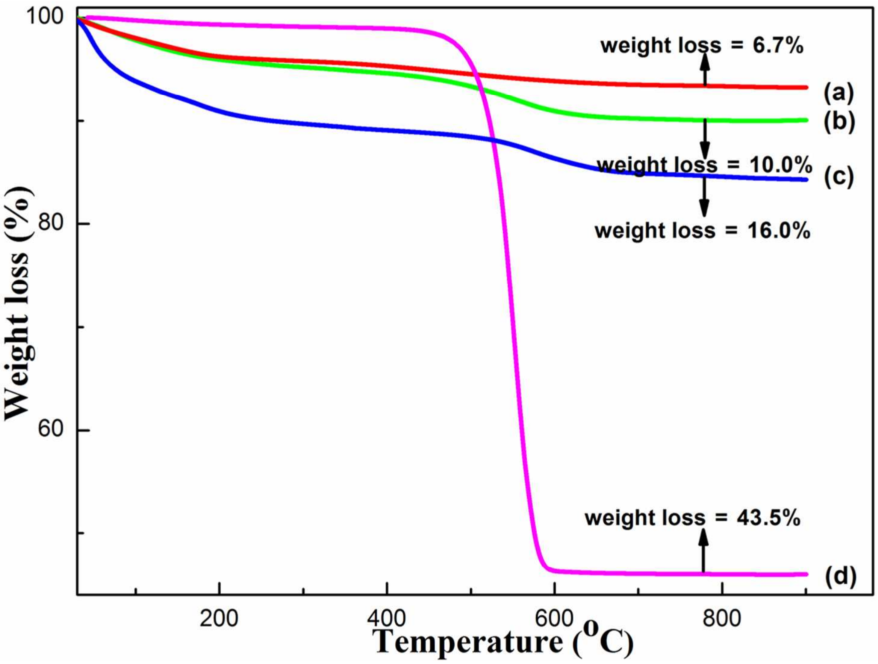
100
80
60
200
400
600
800
Weight loss (%)
Temperature (oC)
weight loss = 6.7%
weight loss = 10.0%
weight loss = 16.0%
weight loss = 43.5%
(a)
(b)
(c)
(d)

Figure 9

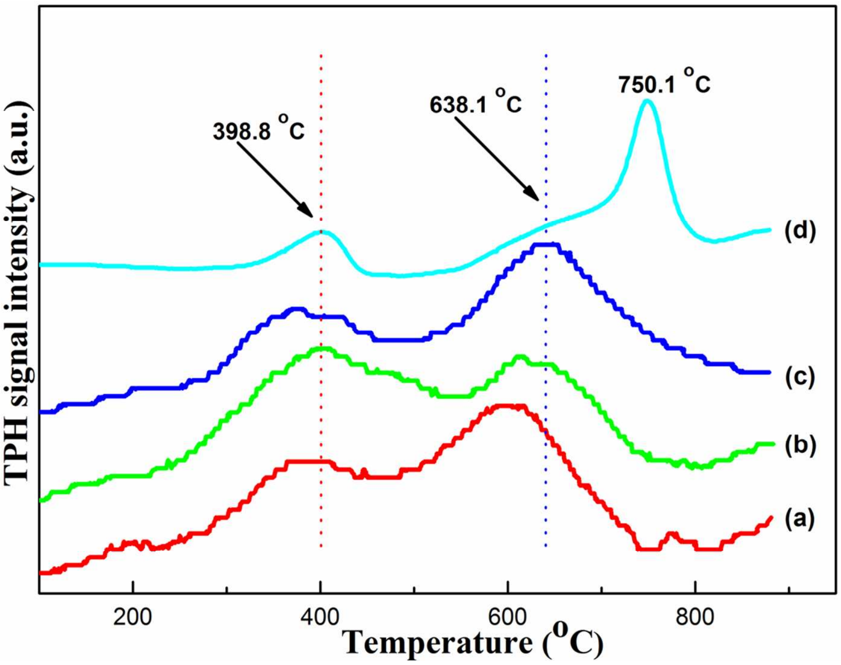
TPH signal intensity (a.u.)
Temperature (°C)
200
400
600
800
398.8 °C
638.1 °C
750.1 °C
(d)
(c)
(b)
(a)

Figure 10

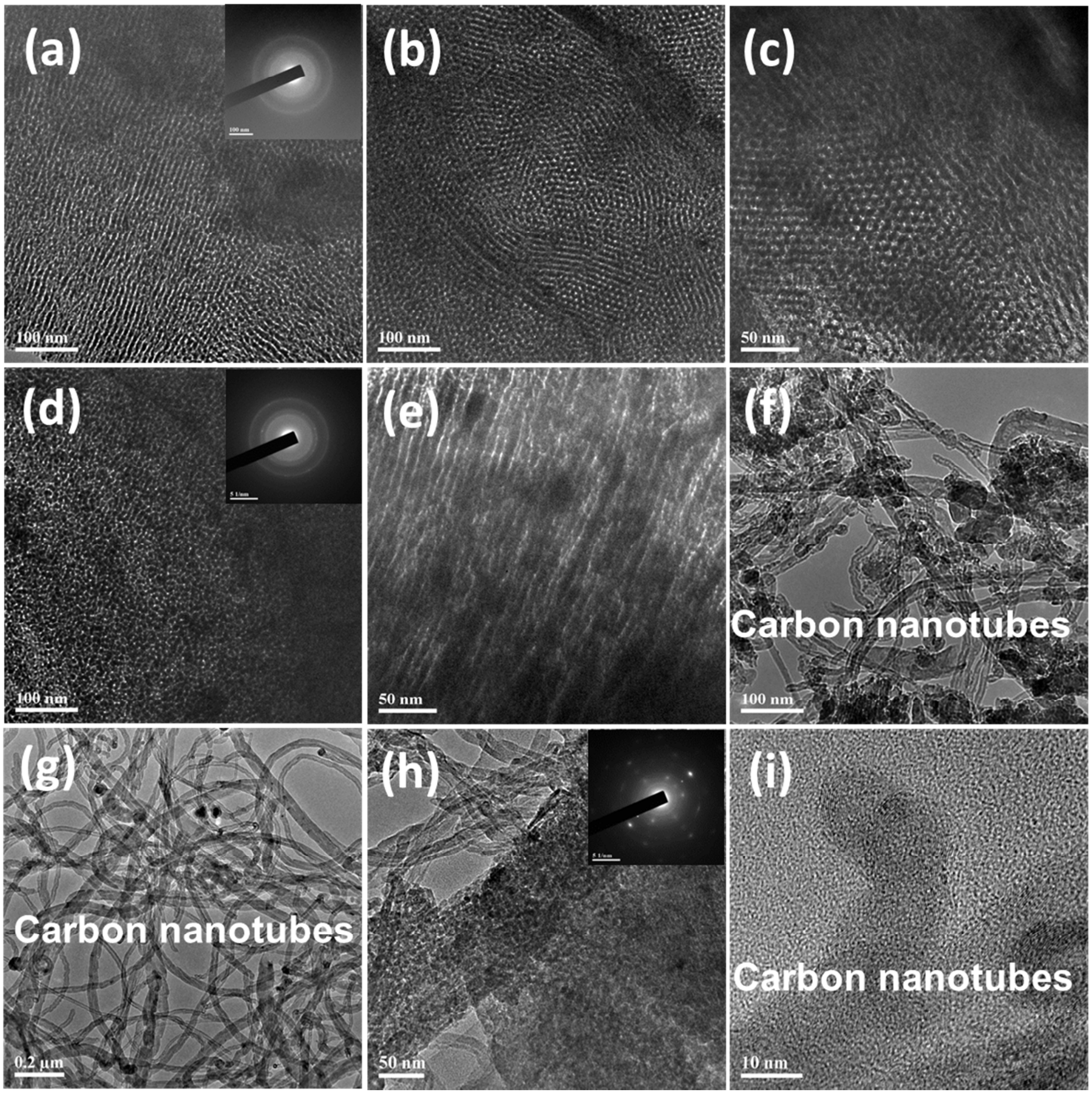
(a)
100 nm
100 nm
(b)
100 nm
(c)
50 nm
(d)
5 1/nm
100 nm
(e)
50 nm
(f)
Carbon nanotubes
100 nm
(g)
Carbon nanotubes
0.2 µm
(h)
5 1/nm
50 nm
(i)
Carbon nanotubes
10 nm

Figure 11